RSC Applied Interfaces

ROYAL SOCIETY OF CHEMISTRY

PAPER

View Article Online
View Journal | View Issue

Cite this: *RSC Appl. Interfaces*, 2026, **3**, 576

Constructing an efficient NiCu single-atom alloy towards acetylene semi-hydrogenation

Xi Zhang,[a] Peng Yin,*[a] Kunze Xue,[a] Tianwei Song,[a] Haiwei Liang [a] and Huan Yan *[b]

Received 4th December 2025,
Accepted 11th February 2026

DOI: 10.1039/d5lf00381d

rsc.li/RSCApplInter

Acetylene semi-hydrogenation is a critical industrial process for purifying raw steam used in polyethylene production. Nickel-based particles have emerged as promising non-noble catalysts for this application. Designing a catalyst with high activity and ethylene selectivity has long been a goal in this field. Single-atom alloys (SAAs) with integrated functions are potential candidates for achieving the two goals simultaneously. Here, we reported a new strategy to construct efficient NiCu SAAs, uncovering two factors for the density of catalytic Ni sites, the alloying degree and exposure degree of Ni. Increasing the reduction temperature could enhance the alloying degree of Ni atoms, and it could also enlarge the particle size of the NiCu SAAs and result in decreased exposure of Ni atoms. The two opposing factors simultaneously led to a volcano-shaped dependence of reaction activity on the reduction temperature. The optimal NiCu single-atom alloys, balancing both key factors, demonstrated notable specific activity and selectivity (29 582 $mL_{C_2H_2}$ min^{-1} g_{Ni}^{-1} and 92.7% ethylene selectivity under 100% acetylene conversion). This research introduced a new strategy for synthesizing efficient SAAs for selective hydrogenation through a straightforward approach.

1. Introduction

Acetylene semi-hydrogenation plays a critical role in the chemical industry by purifying raw steam for polyethylene production, as even trace amounts of acetylene can poison polymerization catalysts.[1–3] In this process, it is essential to hydrogenate acetylene to ethylene, while preventing over-hydrogenation to ethane or polymerization to oligomerization.[4–7] While Pd-based catalysts are commonly used in industry for acetylene semi-hydrogenation, Ni-based catalysts are proposed to replace them due to their lower costs.[8,9] The primary objective of Ni-based catalysts in acetylene semi-hydrogenation is to improve the activity and enhance ethylene selectivity.[10–12]

Bimetallic catalysts are currently widely used catalysts for the semi-hydrogenation of acetylene. The introduction of a second metal not only modulates the coordination environment of the active metal, but also disperses the active metal sites, thereby suppressing over-hydrogenation.[13] Bimetallic catalysts can exist in many structural motifs, such as alloys, dual-atom sites, single-atom-decorated clusters and so on.[14–16] These catalysts each have their own unique advantages. Based on previous research, isolated metal active sites have been proven to enhance ethylene selectivity.[11,17,18] Single-atom alloys (SAAs), where the active doped atoms are isolated within an inactive host metal, offer a promising approach for catalyzing acetylene semi-hydrogenation with high ethylene selectivity.[19–21] When SAAs were employed as hydrogenation catalysts, the group VIII transition metal atoms served as catalytic hydrogenation sites, and the coinage metal host acted as platforms to facilitate hydrogen spillover.[21,22] Additionally, owing to the free-atom-like d-states of guest metal atoms and their unique atomic arrangement,[23–25] SAAs are potential candidates for catalyzing acetylene semi-hydrogenation with high intrinsic activity, thereby breaking the Brønsted–Evans–Polanyi (BEP) scaling relationship.[26,27] However, Ni-based SAAs, which have potential to replace Pd-based catalysts, have not been reported for acetylene semi-hydrogenation.

To bridge the gap between SAA model systems and practical applications, various synthetic approaches have been developed for preparing SAA powder catalysts, including galvanic replacement, sequential reduction and/or incipient wetness co-impregnation.[25] However, most synthetic methods require multiple steps, which hinders their widespread application for synthesizing SAAs. Instead, incipient wetness co-impregnation, as a simple one-pot synthetic approach, is a promising candidate for the scalable synthesis of single-atom alloys.

[a] *Hefei National Research Center for Physical Sciences at the Microscale, Department of Chemistry, University of Science and Technology of China, Hefei 230026, China. E-mail: yp95ustc@mail.ustc.edu.cn*
[b] *State Key Laboratory of Precision and Intelligent Chemistry, School of Chemistry and Materials Science, University of Science and Technology of China, Hefei 230026, China. E-mail: yanhuan1@ustc.edu.cn*

In this study, we synthesized a series of carbon supported NiCu alloys *via* incipient wetness co-impregnation and subjected them to reduction at various temperatures (denoted as $NiCu_x$/C-*T*, where *x* and *T* refer to the atomic ratio of Cu/Ni and reduction temperature). Structural analysis indicated that $NiCu_{500}$/C-300 was the NiCu cluster, and all other samples were identified as NiCu SAAs. Subsequently, a volcano-shaped trend in activity against the reaction temperature was observed, with the peak located at a moderate reduction temperature of 500 °C. To optimize the synthetic method for SAAs *via* incipient wetness co-impregnation, we also investigated the evolution of catalytic site density behind the volcano-shaped trend. Further process studies uncovered that the alloying degree of Ni increased along with the elevated reduction temperature, leading to enhanced apparent catalytic activity. However, the size of alloy particles also increased with increasing reduction temperature, resulting in the embedding of Ni and decrease in apparent catalytic activity. These two temperature-dependent factors, alloying degree and particle size, collectively contributed to the observed volcano trend, where the optimal $NiCu_{500}$/C-*T* could balance the conflicting factors. In this work, $NiCu_{500}$/C-500 could demonstrate significant specific activity (29 582 $mL_{C_2H_2}$ min^{-1} g_{Ni}^{-1}), high ethylene selectivity (92.7%), and stability (89 hours), outperforming previously reported Ni-based catalysts.

2. Experimental

2.1. Materials and chemicals

BP2000 was manufactured by the American company Cabot Corporation. SiO_2 was purchased from Sigma-Aldrich. Nickel(II) chloride hexahydrate ($NiCl_2{\cdot}6H_2O$) and copper(II) chloride dihydrate ($CuCl_2{\cdot}2H_2O$) were purchased from Sinopharm Chemical Reagent as commercial sources. Deionized water (18.2 MΩ cm^{-1}) utilized in all experiments was prepared by passing it through an ultra-pure purification system.

2.2. Synthesis of materials

$NiCu_{500}$/C-300 was prepared using a conventional wet-impregnation method followed by H_2-reduction at 300 °C. Solid-state $NiCl_2{\cdot}6H_2O$ and $CuCl_2{\cdot}2H_2O$ were dissolved in DI water at specific concentrations. In brief, 0.053 mg $NiCl_2$ and 27.44 mg $CuCl_2$ were initially mixed with 200 mg BP2000 in a 250 mL round-bottom flask containing 100 mL DI water. After ultrasonic treatment for 1.5 h, the mixture was stirred for at least 8 h before being dried using a rotary evaporator. The resulting dark powder was heated in a tube furnace at 300 °C under flowing 5% H_2/Ar for 1 h to obtain $NiCu_{500}$/C-300. To obtain $NiCu_{500}$/C-*T* (*T* = 400 °C, 500 °C, and 600 °C), 30 mg $NiCu_{500}$/C-300 was introduced into a fixed-bed flow reactor and heated in 5% H_2/Ar for 2 h, with the temperature ranging from 400 °C to 600 °C. For $NiCu_{500}$/C-800, 30 mg $NiCu_{500}$/C-300 was placed in a tube furnace and heated at 800 °C under flowing 5% H_2/Ar for 2 h. $NiCu_{10}/SiO_2$ was prepared by a similar method.

NiCu SAA/C-*T* (*T* = 300 °C, 400 °C, and 500 °C) was prepared through sequential impregnation and reduction. In a nutshell, 27.44 mg $CuCl_2$ was initially mixed with 200 mg BP2000 in a 250 mL round-bottom flask containing 100 mL DI water. After ultrasonic treatment for 1.5 h, the mixture was stirred for at least 8 h before being dried using a rotary evaporator. The resulting powder was then heated in a tube furnace at 800 °C under flowing 5% H_2/Ar for 2 h to obtain Cu/C-800. All the Cu/C was combined with 0.053 mg of $NiCl_2$ in a 250 mL round-bottom flask containing 100 mL DI water. After ultrasonic treatment for 30 min, the mixture was stirred for at least 8 h before being dried using a rotary evaporator, resulting in Cu/C-800 + Ni. Subsequently, 30 mg Cu/C-800 + Ni was introduced into a fixed-bed flow reactor and heated in 5% H_2/Ar for 50 min, with the temperature ranging from 300 °C to 500 °C, yielding NiCu SAA/C-*T* (*T* = 300 °C, 400 °C, and 500 °C).

Ni/C was prepared using a conventional wet-impregnation method followed by H_2-reduction at 500 °C. Solid-state $NiCl_2{\cdot}6H_2O$ was dissolved in DI water at specific concentrations. In brief, 26.50 mg $NiCl_2$ was initially mixed with 200 mg BP2000 in a 250 mL round-bottom flask containing 100 mL DI water. After ultrasonic treatment for 1.5 h, the mixture was stirred for at least 8 h before being dried using a rotary evaporator. The resulting dark powder was heated in a tube furnace at 500 °C under flowing 5% H_2/Ar for 2 h to obtain Ni/C.

2.3. Characterization of the materials

The XRD patterns were acquired using a Japan Rigaku DMax-γA rotation anode X-ray diffractometer. The wavelength employed in XRD was 1.54178 Å, utilizing graphite monochromatized Cu-K radiation. The TEM image was captured on an H-7650 with an accelerating voltage of 100 kV. The HAADF-STEM images were captured on an FEI Talos F200X with an accelerating voltage of 200 kV. The EDS mapping images were obtained using the Super X-EDS system of the FEI Talos F200X. The DRIFTS experiments were carried out on a Nicolet iS10 spectrometer equipped with a mercury–cadmium–telluride detector and high-temperature *in situ* heating chamber. After loading the $NiCu_{10}/SiO_2$ sample into the cell, it was reduced under 5% H_2 (Ar balance) at 200 °C for 30 min. After cooling the sample to room temperature in Ar, we collected a background spectrum. Subsequently, the sample was exposed to 10% CO in Ar (15 ml min^{-1}) until saturation. Next, the sample was purged with Ar (15 ml min^{-1}) for 10 min to remove the gas-phase CO, after which the DRIFT spectrum was collected. The TPR tests of all catalysts were performed using a Huasi DAS-7000 high-performance dynamic adsorption analyzer equipped with a TCD to measure the consumption of hydrogen. The temperature was set at a ramp rate of 10 °C min^{-1}, and the reducing gas of 5 vol% H_2 balanced N_2 was set at a flow rate of 50 mL min^{-1}.

2.4. Acetylene hydrogenation testing

Acetylene hydrogenation testing in excess ethylene was conducted in a fixed-bed flow reactor. Before the hydrogenation testing, 30 mg $NiCu_{500}$/C-300, $NiCu_{500}$/C-800 and Ni/C were reduced at 300 °C under flowing 5% H_2/Ar for 30 min. Other catalysts were produced in the fixed-bed flow reactor under flowing 5% H_2/Ar and were not exposed to air. After cooling to room temperature, a reactant gas mixture (0.5 vol% C_2H_2, 5 vol% H_2, 20 vol% C_2H_4, and balance N_2) at a flow rate of 20 mL min^{-1} was fed into the reactor. The composition of the reactants and products was analyzed online using a GC9790Plus gas chromatograph equipped with an FID. The acetylene conversion rate, ethylene selectivity, selectivity towards other products, and specific activity were calculated using the following equations:

$$C_2H_2 \text{ conversion rate} = \frac{[C_2H_2]_{inlet} - [C_2H_2]_{outlet}}{[C_2H_2]_{inlet}} \times 100\%$$

$$C_2H_4 \text{ selectivity} = 1 - \frac{[C_2H_6]_{outlet} - [C_2H_6]_{inlet} + 2 \times [C_4]_{outlet}}{[C_2H_2]_{inlet} - [C_2H_2]_{outlet}} \times 100\%$$

$$C_2H_6 \text{ selectivity} = \frac{[C_2H_6]_{outlet} - [C_2H_6]_{inlet}}{[C_2H_2]_{inlet} \times [C_2H_2]_{outlet}} \times 100\%$$

$$C_4 \text{ selectivity} = \frac{2 \times [C_4]_{outlet}}{[C_2H_2]_{inlet} - [C_2H_2]_{outlet}} \times 100\%$$

$$\text{Specific activity} = \frac{C_2H_2\,(\text{in feed}) \times C_2H_2 \text{ conversion rate}}{\text{mass of Ni}}$$

3. Results and discussion

3.1. Structure characterization of catalysts

$NiCu_{500}$/C-T was prepared through incipient wetness co-impregnation and thermal reduction. The weight loadings of Ni and Cu in $NiCu_{500}$/C-T were 0.013 and 5.5 wt%, respectively, with an atomic ratio of ~0.002 (Table S1), determined by inductively coupled plasma atomic emission spectrometry (ICP-AES). To identify the phase of $NiCu_{500}$/C-T, we resorted to X-ray diffraction (XRD), as shown in Fig. 1(a–e). In the XRD pattern of $NiCu_{500}$/C-300, no visible plane diffraction peaks assigned to facets of metal or metallic nanoparticles were observed. Combining this with the high-angle annular dark-field scanning transmission electron microscopy (HAADF-STEM) image of $NiCu_{500}$/C-300 shown in Fig. 1(f), we could infer that the main state of NiCu in $NiCu_{500}$/C-300 was in an uncrystallized cluster. Other XRD patterns of $NiCu_{500}$/C-T aligned with that of Cu, suggesting that the structures of particles in $NiCu_{500}$/C-T (T = 400 °C, 500 °C, 600 °C, and 800 °C) were identical to the pure Cu. To investigate the morphology of $NiCu_{500}$/C-T, we resorted to HAADF-STEM, as shown in Fig. 1(f–j) and S1 in the SI. Apart from $NiCu_{500}$/C-300, other HAADF-STEM images illustrated that the particle size of $NiCu_{500}$/C-T increased with the elevated reduction temperature. As shown in Fig. 1(k), elemental mapping with energy-dispersive X-ray spectroscopy (EDS) indicated that Ni was uniformly distributed in a randomly chosen particle in $NiCu_{500}$/C-500, with Cu being its main component. The calculation was based on the K_a of Ni and Cu, and the atomic ratio was 0.0022 calculated with the peak area ratio (peak area of Ni: 1.04, k-factor was 4.18; peak area of Cu:

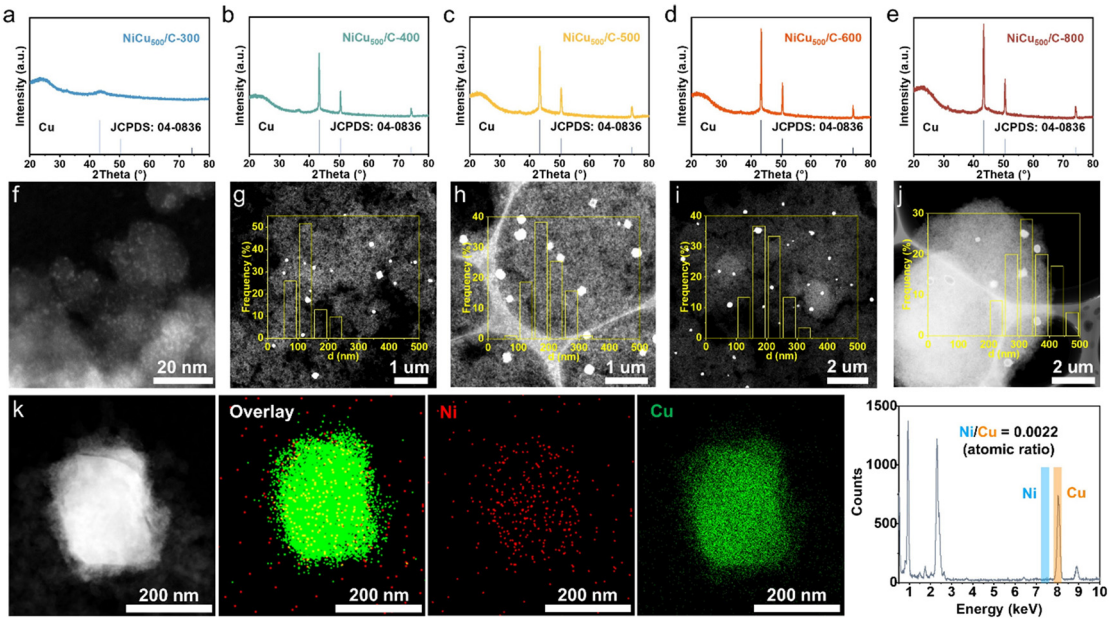

Fig. 1 Structural characterization of $NiCu_{500}$/C-T. (a–e) XRD patterns of $NiCu_{500}$/C-T (T = 300 °C, 400 °C, 500 °C, 600 °C, and 800 °C). (f–j) HAADF-STEM images of $NiCu_{500}$/C-T (T = 300 °C, 400 °C, 500 °C, 600 °C, and 800 °C). The inserts are the corresponding statistics of particle diameter distribution. (k) The EDS elemental mapping of $NiCu_{500}$/C-500 and the corresponding elemental ratio of Ni and Cu elements.

583.35, *k*-factor was 5.15). Considering the disproportionate atomic ratio of NiCu (Fig. 1(k)), the NiCu SAA was potentially formed in $NiCu_{500}$/C-500. The SAA structures of other $NiCu_{500}$/C-*T* samples (*T* = 400 °C, 600 °C, and 800 °C) were also demonstrated by the EDS elemental mapping shown in Fig. S2 in the SI. To determine whether Ni ensembles exist, we performed the CO-DRIFTS of $NiCu_{10}/SiO_2$ (CO-DRIFTS characterization was not conducted on the carbon-supported NiCu due to the strong infrared absorption of the carbon support, which would severely interfere with the signal) as shown in Fig. S3 in the SI. The linear CO absorption band on Ni ensembles was at 2055 cm^{-1},[28] which was absent, indicating that the presence of Ni ensembles could be excluded. We could infer that there were no Ni ensembles in the $NiCu_{500}$/C-*T* (*T* = 400 °C, 600 °C, and 800 °C) based the CO-DRIFTS of $NiCu_{10}/SiO_2$.

3.2. Catalytic tests of acetylene semi-hydrogenation

Acetylene semi-hydrogenation performance over $NiCu_{500}$/C-*T* was tested in a fixed-bed reactor with $C_2H_4:H_2:C_2H_2$ = 40 : 10 : 1. Fig. 2(a) illustrates the C_2H_2 conversion and C_2H_4 selectivity with respect to the reaction temperature with all $NiCu_{500}$/C-*T* samples, where a clear trend of catalytic semi-hydrogenation was observed. Among them, $NiCu_{500}$/C-500 offered the highest C_2H_2 conversion rate at 91.7% at 240 °C, while $NiCu_{500}$/C-300 and $NiCu_{500}$/C-800 showed zero conversion rates across the entire temperature range. $NiCu_{500}$/C-400 and $NiCu_{500}$/C-600 provided a moderate activity, achieving 46.9% and 48.2% conversion rates at 240 °C, respectively. Due to the identical Ni loading and catalyst mass among the $NiCu_{500}$/C-*T* series, the trend observed in the C_2H_2 conversion rate reveals the intrinsic activity (Ni specific activity). In Fig. 2(b), Ni specific activity (240 °C) was plotted against the reduction temperature of $NiCu_{500}$/C-*T*, revealing a volcano trend with a peak at a moderate reduction temperature of 500 °C ($NiCu_{500}$/C-*T*). Regarding C_2H_4 selectivity, $NiCu_{500}$/C-400, $NiCu_{500}$/C-500, and $NiCu_{500}$/C-600 all exhibited selectivity higher than 90%. As the C_2H_2 conversion rate was zero, C_2H_4 selectivity for $NiCu_{500}$/C-300 and $NiCu_{500}$/C-800 was not discussed. The lowest selectivity value was observed for $NiCu_{500}$/C-500 at 240 °C, still achieving 91.9% with a C_2H_2 conversion of 91.7%.

Considering the outstanding selectivity and activity among $NiCu_{500}$/C-*T*, we assessed the stability of $NiCu_{500}$/C-500 and examined the selectivity to primary by-products, C_2H_6 and C_4 (Fig. 2(c)). The catalyst deactivation in the semi-hydrogenation of C_2H_2 was ascribed to the formation of green oil, a polymer of C4.[6,29,30] Despite a low C4 selectivity (7.8%), $NiCu_{500}$/C-500 maintained stability for 89 hours, with a C_2H_2 conversion exceeding 94% and consistent C_2H_4 selectivity. After the stability test, the morphology of the catalyst remained basically unchanged, and the Ni was kept isolated according to the EDS mapping (Fig. S4 in the SI). Notably, C_2H_4 selectivity remained above 91% even when the C_2H_2 conversion reached 100%. In an atmosphere with

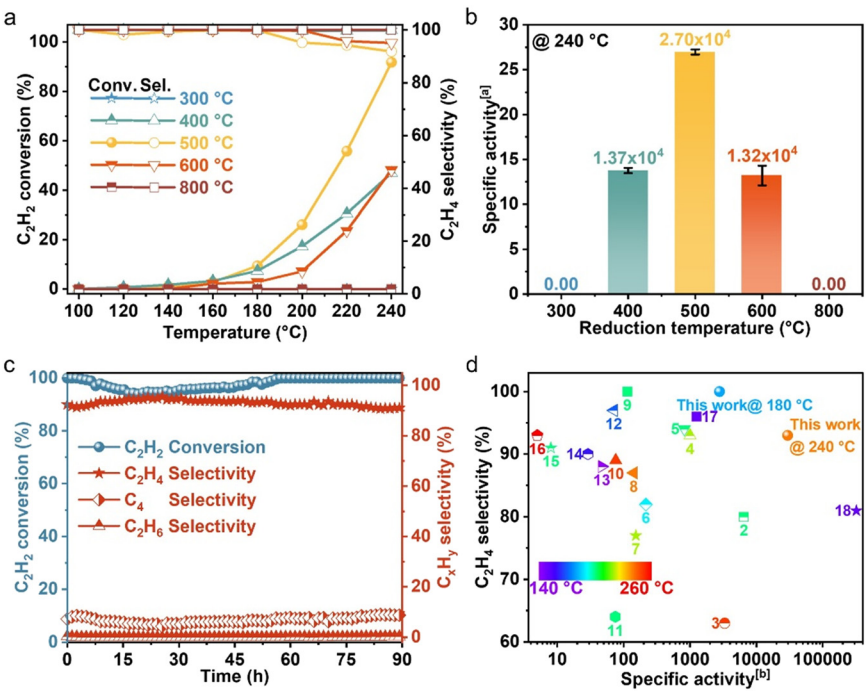

Fig. 2 Catalytic performances for acetylene hydrogenation. (a) Acetylene conversion rate and ethylene selectivity as functions of temperature over $NiCu_{500}$/C-*T* (*T* = 300 °C, 400 °C, 500 °C, 600 °C, and 800 °C). (b) Specific activity of $NiCu_{500}$/C-*T* (*T* = 300 °C, 400 °C, 500 °C, 600 °C, and 800 °C) (@ 240 °C). (c) Acetylene conversion rate, ethylene selectivity, and selectivity towards other products with the time on stream over $NiCu_{500}$/C-500. (d) Specific activity and ethylene selectivity for $NiCu_{500}$/C-500 and in the literature (shown in Table S2). [a]Unit: 10^3 $mL_{C_2H_2}$ min^{-1} g_{Ni}^{-1}. [b]Unit: $mL_{C_2H_2}$ min^{-1} g_{Ni}^{-1}.

excess C_2H_4 and H_2 (the excess H_2 is added to achieve high C_2H_2 conversion), it's challenging for the catalysts to avoid catalyzing C_2H_4 to C_2H_6.[31–33] However, when the C_2H_2 conversion reached 100%, the C_2H_6 selectivity over $NiCu_{500}$/C-500 remained below 1%, confirming the high capability of $NiCu_{500}$/C-500 in suppressing over-hydrogenation to C_2H_6. As a comparison, pure Ni particles supported by carbon (denoted as Ni/C) were synthesized (Fig. S5 in the SI) and tested (Fig. S6 in the SI). Compared with the pure Ni nanoparticles, at the 100% C_2H_2 conversion, $NiCu_{500}$/C-500 demonstrated higher C_2H_4 selectivity, suppressing the over hydrogenation.

Despite a low Ni loading of 0.013 wt%, $NiCu_{500}$/C-500 exhibited a significant C_2H_2 conversion, demonstrating the superior specific activity of $NiCu_{500}$/C-500 at high C_2H_4 selectivity (Fig. 2(d)). Comparing the catalytic performance of $NiCu_{500}$/C-500 with other reported Ni-based catalysts in terms of specific activity and ethylene selectivity, $NiCu_{500}$/C-500 could offer a high specific activity (29 582 $mL_{C_2H_2}$ min^{-1} g_{Ni}^{-1}) with high C_2H_4 selectivity. Considering the temperature effect on activity, we also presented a low-temperature specific activity (180 °C) of $NiCu_{500}$/C-500, which still provided superior specific activity and ethylene selectivity. Consequently, the catalyst design based on NiCu SAAs achieved remarkably high catalytic activity and selectivity.

3.3. Investigation on the evolution of catalytic site density

To elucidate the individual roles of the dopant and host metals in NiCu single-atom alloys (SAAs), we prepared two reference catalysts: carbon-supported Ni single atoms and Cu particles. The metal loadings (0.013 wt% Ni and 5.7 wt% Cu) were designed to match those in the $NiCu_{500}$/C-*T* SAA. We then compared their catalytic performance with $NiCu_{500}$/C-500. Compared with $NiCu_{500}$/C-500 (Fig. 3(a)), Ni single atoms and/or Cu particles exhibited extremely low activity for the C_2H_2 semi-hydrogenation. This observation underscored the indispensable roles of Ni single atoms and Cu particles in acetylene semi-hydrogenation within NiCu SAAs. In the NiCu SAA, Ni atoms possibly functioned as sites of hydrogen dissociation, with Cu facets facilitating hydrogen atom migration and C_2H_2 hydrogenation, as illustrated in Fig. 3(b). To validate this function, we conducted temperature programmed reduction (TPR) experiments on the fresh sample, as shown in Fig. 3(c). H_2-TPR indicates that the monometallic Ni (Ni/C) could be reduced at around 410 °C. The H_2-TPR profile for the monometallic Cu (Cu/C) contains two reduction peaks at 424 °C and 655 °C, which were attributed to the reduction of Cu(II) species to Cu(I) and then to Cu(0), respectively.[34] Notably, the addition of a small amount of Ni (atomic ratio of Ni : Cu = 1 : 50, denoted as $NiCu_{50}$) resulted in a lower temperature peak compared to Cu/C. The significant shift of the H_2-TPR peak of Cu reduction to a lower temperature in $NiCu_{50}$/C can be attributed to the hydrogen spillover in the NiCu SAA.[34] Combining the TPR results and previous research,[19,35] within NiCu SAAs, Ni single atoms served as sites of hydrogen dissociation, and Cu facets facilitated hydrogen spillover and C_2H_2 hydrogenation.

After confirming the roles of Cu–Ni in the NiCu SAA, we further study the two opposing factors, the alloying degree

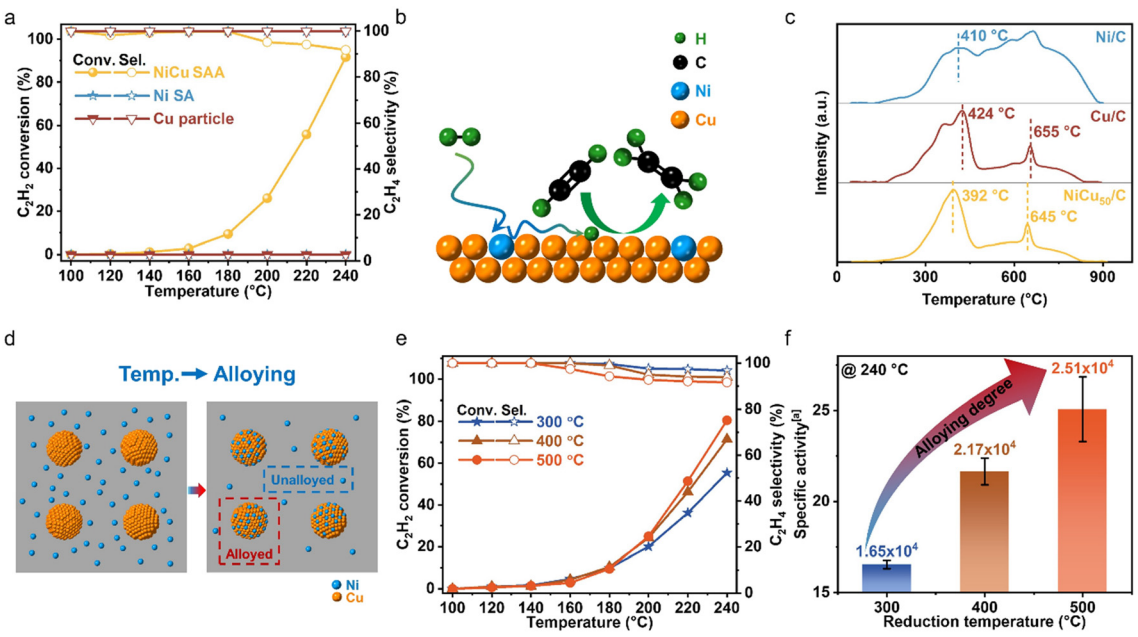

Fig. 3 Investigating the active sites and influence of temperature on the alloying degree of Ni atoms. (a) Comparison of catalytic activity between the NiCu single-atom alloy, Ni single atom, and Cu particles. (b) The illustration of the role of doped Ni atoms and the Cu substrate. (c) TPR profiles of Ni/C, Cu/C and $NiCu_{50}$/C. (d) The illustration of investigating experimental design. (e) Acetylene conversion and ethylene selectivity as functions of temperature over NiCu SAA/C-*T* (*T* = 300 °C, 400 °C, and 500 °C). (f) Specific activity of NiCu SAA/C-*T* (*T* = 300 °C, 400 °C, and 500 °C) (@ 240 °C). [a]Unit: 10^3 $mL_{C_2H_2}$ min^{-1} g_{Ni}^{-1}.

and exposure degree of Ni atoms, to identify the formation process of the optimized catalysts. When there is a higher alloying degree with lower Ni atom encapsulation, a greater density of catalytic sites is achieved due to the change of the local coordination environment during the alloying process.[13,36]

To examine how the alloying degree evolved with reduction temperature and exclude the effect of Ni atom encapsulation, we synthesized a series of $NiCu_{500}$/C catalysts *via* incipient wetness sequential impregnation, using Cu/C that had been pre-reduced at 800 °C for 2 hours as the 'pre-support', as illustrated in Fig. 3(d). To minimize changes in the Cu particle structure, the sequentially impregnated $NiCu_{500}$/C samples were reduced for only 50 minutes at 300, 400, and 500 °C, and were denoted as NiCu SAA/C-*T*, where *T* indicated the reduction temperature. XRD analysis of NiCu SAA/C-*T* (*T* = 300, 400, and 500 °C) confirmed that no significant sintering had occurred compared to Cu/C reduced at 800 °C, as shown in Fig. S7 in the SI. As shown in Fig. 3(e), the C_2H_2 conversion rate increased with reduction temperature. Moreover, the C_2H_4 selectivity remained comparable to that of $NiCu_{500}$/C-500, suggesting that alloyed Ni atoms retained their good dispersion in the NiCu SAA nanoparticles. We plotted the specific activity of Ni atoms at 240 °C as a function of reduction temperature, which showed a positive correlation, as shown in Fig. 3(f). This trend indicated that higher reduction temperatures promoted the migration of Ni atoms from the support to Cu particles, facilitating the formation of active catalytic sites with higher alloying degree. Then, we studied the second factor for Ni catalytic sites in the NiCu SAA, the exposure degree of Ni atoms. As illustrated in Fig. 4(a), the particle size of the alloy increased with the increasing reduction temperature. This increase in particle size was possibly accompanied by a decrease in Ni exposure, as depicted in Fig. 4(b). To validate this speculation, we prepared $NiCu_{500}$/C using two methods, incipient wetness co-impregnation and incipient wetness sequential impregnation (denoted as $NiCu_{500}$/C-800 and Cu/C-800 + Ni, respectively), and evaluated their catalytic performance. As shown in Fig. 4(c), the Cu/C-800 + Ni catalyst exhibited higher activity than $NiCu_{500}$/C-800. With similar particle sizes for both catalysts (Fig. S7 and S8 in the SI), the low hydrogenation activity of $NiCu_{500}$/C-800 was attributed to the limited exposure degree of Ni after high-temperature (800 °C) reduction. What's more, the exposure degree of Ni could also be determined by CO-DRIFTS (Fig. S3 in the SI). As the reduction temperature increased, the intensity of the peak of adsorbed CO on Ni gradually decreased, indicating a reduction in the surface Ni content. Consequently, the exposure degree of Ni atoms was inversely proportional to the reduction temperature, thereby negatively affecting catalytic activity. As shown in Fig. 4d, two key factors significantly affected the activity of NiCu SAAs, the alloying degree and exposure degree of Ni atoms. The combined influence of these two factors ultimately resulted in the volcano-shaped trend of the reaction activity against reduction temperature.

4. Conclusions

In summary, we have elucidated the process of NiCu single-atom alloy site evolution and optimized NiCu SAAs for acetylene semi-hydrogenation *via* a straightforward approach. With elevated reduction temperature, the alloying degree of Ni increased, and the size of alloy particles also increased along with a decrease in the exposure degree of Ni. Both

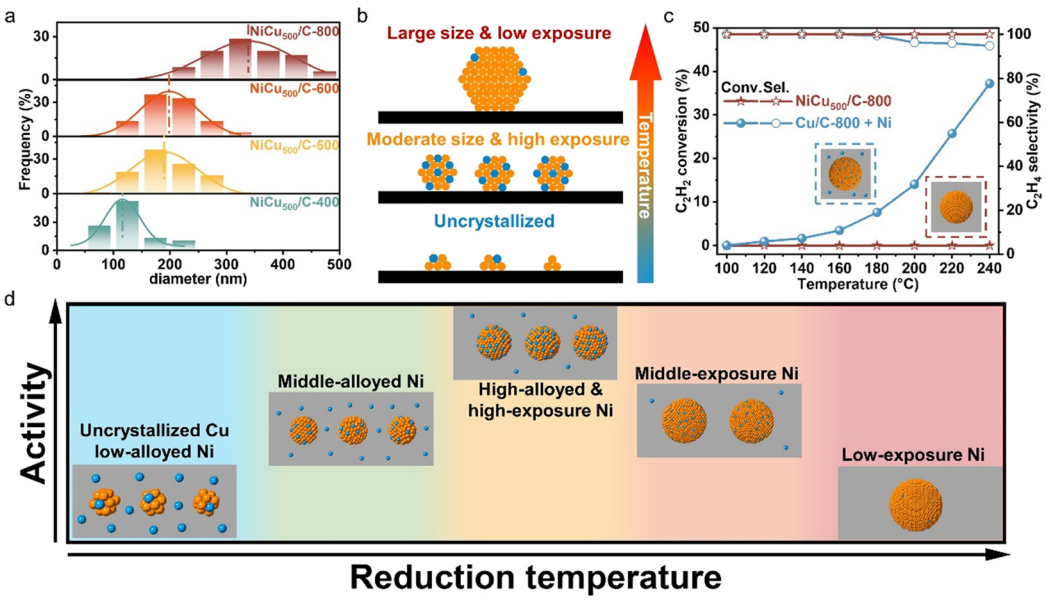

Fig. 4 Investigating the influence of temperature on the particle size. (a) Particle diameter distribution of $NiCu_{500}$/C-*T* (*T* = 400 °C, 500 °C, 600 °C, and 800 °C). (b) Proposed particle evolution diagram in $NiCu_{500}$/C-*T*. (c) Confirmation of the decreased exposure degree of Ni atoms in $NiCu_{500}$/C-800. (d) The illustration of the morphological changes of $NiCu_{500}$/C-*T*.

factors jointly contributed to the observed volcano trend. $NiCu_{500}$/C-500 exhibited an optimal alloying degree and exposure degree of Ni atoms, resulting in superior specific activity and selectivity in acetylene semi-hydrogenation. This strategy of catalyst design offers inspiration for developing efficient SAAs through a straightforward approach.

Author contributions

X. Z., P. Y., and H. Y. conceived the idea. X. Z. and P. Y. jointly prepared the catalysts and tested the catalytic performance. X. Z. conducted the structural characterization of the catalyst. X. Z., P. Y., K.-Z. X, T.-W. S. and H. W. L. jointly conducted the data analysis and literature research. X. Z., P. Y., and H. Y. wrote and revised the paper. All the authors have approved the final manuscript.

Conflicts of interest

There are no conflicts to declare.

Data availability

The data supporting this study are available in the paper and the supplementary information (SI). All other relevant source data are available from the corresponding authors upon reasonable request.

Supplementary information: the SI includes the structural characterization not shown in the main article and performance comparison. See DOI: https://doi.org/10.1039/d5lf00381d.

Acknowledgements

The authors acknowledge the funding support from the National Key Research and Development Program of China (Grant 2023YFA1508200), the fund of USTC start-up grant (KY2060000213 and KY2060000204), and the National Natural Science Foundation of China (GG2060007005).

References

1 B. Lou, H. Kang, W. Yuan, L. Ma, W. Huang, Y. Wang, Z. Jiang, Y. Du, S. Zou and J. Fan, *ACS Catal.*, 2021, **11**, 6073–6080.
2 S. Wei, X. Liu, C. Wang, X. Liu, Q. Zhang and Z. Li, *ACS Nano*, 2023, **17**, 14831–14839.
3 R. Huang, M. Xia, Y. Zhang, C. Guan, Y. Wei, Z. Jiang, M. Li, B. Zhao, X. Hou, Y. Wei, Q. Chen, J. Hu, X. Cui, L. Yu and D. Deng, *Nat. Catal.*, 2023, **6**, 1005–1015.
4 J. Ma, F. Xing, Y. Nakaya, K. I. Shimizu and S. Furukawa, *Angew. Chem., Int. Ed.*, 2022, **61**, e202200889.
5 F. Huang, Y. Deng, Y. Chen, X. Cai, M. Peng, Z. Jia, J. Xie, D. Xiao, X. Wen, N. Wang, Z. Jiang, H. Liu and D. Ma, *Nat. Commun.*, 2019, **10**, 4431.
6 X. Ge, Y. Cao, K. Yan, Y. Li, L. Zhou, S. Dai, J. Zhang, X. Gong, G. Qian, X. Zhou, W. Yuan and X. Duan, *Angew. Chem., Int. Ed.*, 2022, **61**, e202215225.
7 Z. Almisbaa, H. A. Aljama, K. Almajnouni, L. Cavallo and P. Sautet, *ACS Catal.*, 2023, **13**, 7358–7370.
8 F. Studt, F. Abild-Pedersen, T. Bligaard, R. Z. Sorensen, C. H. Christensen and J. K. Norskov, *Science*, 2008, **320**, 1320–1322.
9 M. Armbruster, K. Kovnir, M. Friedrich, D. Teschner, G. Wowsnick, M. Hahne, P. Gille, L. Szentmiklosi, M. Feuerbacher, M. Heggen, F. Girgsdies, D. Rosenthal, R. Schlogl and Y. Grin, *Nat. Mater.*, 2012, **11**, 690–693.
10 Y. Liu, X. Liu, Q. Feng, D. He, L. Zhang, C. Lian, R. Shen, G. Zhao, Y. Ji, D. Wang, G. Zhou and Y. Li, *Adv. Mater.*, 2016, **28**, 4747–4754.
11 Y. Cao, H. Zhang, S. Ji, Z. Sui, Z. Jiang, D. Wang, F. Zaera, X. Zhou, X. Duan and Y. Li, *Angew. Chem., Int. Ed.*, 2020, **59**, 11647–11652.
12 X. Ge, M. Dou, Y. Cao, X. Liu, Q. Yuwen, J. Zhang, G. Qian, X. Gong, X. Zhou, L. Chen, W. Yuan and X. Duan, *Nat. Commun.*, 2022, **13**, 5534.
13 Z. Wang, L. Shang, H. Yang, Y. Zhao, G. I. N. Waterhouse, D. Li, R. Shi and T. Zhang, *Adv. Mater.*, 2023, **35**, 2303818.
14 C. Sui, W. Dong, M. Wang, F. Huang, S. Xiang, H. Wang, J. Chen, C. Li, M. Peng, N. Wang, G. Sun, D. Ma and H. Liu, *J. Am. Chem. Soc.*, 2025, **147**, 19808–19816.
15 F. Huang, M. Peng, Y. Chen, X. Cai, X. Qin, N. Wang, D. Xiao, L. Jin, G. Wang, X. D. Wen, H. Liu and D. Ma, *J. Am. Chem. Soc.*, 2022, **144**, 18485–18493.
16 Y. Ge, X. Qin, A. Li, Y. Deng, L. Lin, M. Zhang, Q. Yu, S. Li, M. Peng, Y. Xu, X. Zhao, M. Xu, W. Zhou, S. Yao and D. Ma, *J. Am. Chem. Soc.*, 2020, **143**, 628–633.
17 Y. Niu, X. Huang, Y. Wang, M. Xu, J. Chen, S. Xu, M. G. Willinger, W. Zhang, M. Wei and B. Zhang, *Nat. Commun.*, 2020, **11**, 3324.
18 Y. Niu, Y. Wang, J. Chen, S. Li, X. Huang, M.-G. Willinger, W. Zhang, Y. Liu and B. Zhang, *Sci. Adv.*, 2022, **8**, eabq5751.
19 G. Kyriakou, M. B. Boucher, A. D. Jewell, E. A. Lewis, T. J. Lawton, A. E. Baber, H. L. Tierney, M. Flytzani-Stephanopoulos and E. C. H. Sykes, *Science*, 2012, **335**, 1209–1212.
20 L. Jiang, K. Liu, S. F. Hung, L. Zhou, R. Qin, Q. Zhang, P. Liu, L. Gu, H. M. Chen, G. Fu and N. Zheng, *Nat. Nanotechnol.*, 2020, **15**, 848–853.
21 G. Giannakakis, M. Flytzani-Stephanopoulos and E. C. H. Sykes, *Acc. Chem. Res.*, 2019, **52**, 237–247.
22 R. Reocreux and M. Stamatakis, *Acc. Chem. Res.*, 2022, **55**, 87–97.
23 M. T. Darby, M. Stamatakis, A. Michaelides and E. C. H. Sykes, *J. Phys. Chem. Lett.*, 2018, **9**, 5636–5646.
24 M. T. Greiner, T. E. Jones, S. Beeg, L. Zwiener, M. Scherzer, F. Girgsdies, S. Piccinin, M. Armbruester, A. Knop-Gericke and R. Schloegl, *Nat. Chem.*, 2018, **10**, 1008–1015.
25 R. T. Hannagan, G. Giannakakis, M. Flytzani-Stephanopoulos and E. C. H. Sykes, *Chem. Rev.*, 2020, **120**, 12044–12088.
26 T. Zhang, A. G. Walsh, J. Yu and P. Zhang, *Chem. Soc. Rev.*, 2021, **50**, 569–588.
27 Q. Gao, Z. Yan, W. Zhang, H. S. Pillai, B. Yao, W. Zang, Y. Liu, X. Han, B. Min, H. Zhou, L. Ma, B. Anaclet, S. Zhang, H. Xin, Q. He and H. Zhu, *J. Am. Chem. Soc.*, 2023, **145**, 19961–19968.

28 J. Shan, N. Janvelyan, H. Li, J. Liu, T. M. Egle, J. Ye, M. M. Biener, J. Biener, C. M. Friend and M. Flytzani-Stephanopoulos, *Appl. Catal., B*, 2017, **205**, 541–550.
29 E. Vignola, S. N. Steinmann, A. Al Farra, B. D. Vandegehuchte, D. Curulla and P. Sautet, *ACS Catal.*, 2018, **8**, 1662–1671.
30 X. Shi, Y. Lin, L. Huang, Z. Sun, Y. Yang, X. Zhou, E. Vovk, X. Liu, X. Huang, M. Sun, S. Wei and J. Lu, *ACS Catal.*, 2020, **10**, 3495–3504.
31 G. X. Pei, X. Y. Liu, X. Yang, L. Zhang, A. Wang, L. Li, H. Wang, X. Wang and T. Zhang, *ACS Catal.*, 2017, **7**, 1491–1500.
32 G. X. Pei, X. Y. Liu, A. Wang, A. F. Lee, M. A. Isaacs, L. Li, X. Pan, X. Yang, X. Wang, Z. Tai, K. Wilson and T. Zhang, *ACS Catal.*, 2015, **5**, 3717–3725.
33 R. Shi, Z. Wang, Y. Zhao, G. I. N. Waterhouse, Z. Li, B. Zhang, Z. Sun, C. Xia, H. Wang and T. Zhang, *Nat. Catal.*, 2021, **4**, 565–574.
34 S.-L. Xu, P. Yin, L.-J. Zuo, S.-Y. Yin, M. Zuo, W. Zhang, X.-Z. Fu and H.-W. Liang, *Inorg. Chem. Front.*, 2023, **10**, 3359–3366.
35 F. R. Lucci, J. Liu, M. D. Marcinkowski, M. Yang, L. F. Allard, M. Flytzani-Stephanopoulos and E. C. Sykes, *Nat. Commun.*, 2015, **6**, 8550.
36 C.-L. Yang, L.-N. Wang, P. Yin, J. Liu, M.-X. Chen, Q.-Q. Yan, Z.-S. Wang, S.-L. Xu, S.-Q. Chu, C. Cui, H. Ju, J. Zhu, Y. Lin, J. Shui and H.-W. Liang, *Science*, 2021, **374**, 459–464.